Int J Environ Res (2024) 18:13
https://doi.org/10.1007/s41742-023-00563-5

RESEARCH PAPER

Gd_2O_3/CdS Nanocomposites were Synthesized for Photocatalytic Elimination of Methyl Blue (MB) Dye Under Visible Light Irradiation

Dalia Abdrabou[1] · Mohamed Khalaf Ahmed[2] · Sherif A. Khairy[3] · Tharwat Mahmoud El-Sherbini[3,4]

Received: 19 August 2023 / Revised: 2 November 2023 / Accepted: 16 December 2023 / Published online: 12 February 2024
© The Author(s) 2024

Abstract

Water contamination with hazardous dyes is a serious environmental issue that concerns humanity. A green technology to resolve this issue is the use of highly efficient photocatalysts under visible light to degrade these organic molecules. Adding composite and modifying shape and size on semiconductor materials are attempts to improve the efficacy of these compositions. The optical, microstructural and photocatalytic features of the compositions were investigated by several characterization procedures such as XRD, XPS, SEM, and TEM. Here, modifies Scherrer equation, Williamson–Hall (W–H), and Halder–Wagner method (H–W) have been used to investigate the crystal size and the micro-strain from the XRD peak broadening analysis. The average crystal size according to Modified Scherrer's formula was 6.04–10.46 nm for pristine CdS and CdS/Gd2O3@GO, respectively. While the micro-strain (ε) corresponds to 3.88, 4.63, 4.03, and 4.15 for CdS, Gd_2O_3, CdS/Gd_2O_3, and CdS/Gd_2O_3@GO. It was also shown that the modest difference in average crystal size acquired by the Modified Scherrer and Halder–Wagner (HW) forms was related to differences in average particle size classification. As a result, the Halder–Wagner method was accurate in estimating crystallite size for the compositions. The average roughness is slightly changed from 4.4 to 4.24 nm for CdS/Gd_2O_3 and CdS/Gd_2O_3@GO, respectively. A kinetics investigation further revealed that the photocatalytic degradation of MB dyes was accompanied by a Langmuir isotherm and a pseudo-second-order reaction rate. The highest adsorption capacity (qe) determined for (type 1) CdS, Gd_2O_3, CdS/Gd_2O_3, and CdS/Gd_2O_3@GO adsorption was 5, 0.067, 0.027, and 0.012 mgg^{-1}, respectively. The R^2 values originated from the pseudo-second-order (type 2) for CdS, Gd_2O_3, CdS/Gd_2O_3, and CdS/ Gd_2O_3@GO were 0.904, 0,928, 0.825, and 0.977. As a result, the initial sorption rate (h) is altered between types 1 and 2. In type 2, the pseudo-second-order rate constant (k2) ranges from 0.005 for CdS to 0.011 for CdS/Gd_2O_3@GO. The Langmuir Hinshelwood and pseudo-second-order kinetic models describe the photodegradation process. The results demonstrate that the developed compositions can be used as a long-term substance for dye removal.

Keywords Cadmium sulfide · Gadolinium oxide · Organic pollutants · Photocatalysis

Introduction

Water contamination is crucial issues worldwide due to the increasing utilize of organic compositions, particularly in the industrial source such as textile, agricultural, paper, leather, pharmaceutical, printing, and tannery (Liyun et al. 2023). Natural water is mostly classified into groundwater and surface water (Gopalan Saianand et al. 2023). Surface water implicates rivers, reservoirs, lakes, streams, and ponds, each with its own dynamics and exposed to both land surfaces and the atmosphere (Piyawan Nuengmatcha et al. 2023). Water can include toxic compositions such as organic compounds, metalloids, and metals (2023). Contamination is realized by the concentration and existence of these

✉ Dalia Abdrabou
dalia.saad@must.edu.eg

1 Misr University for Science and Technology, 6 October, Giza 12566, Egypt

2 Department of Physics, Faculty of Science, Suez University, Suez 43518, Egypt

3 Department of Physics, Faculty of Science, Cairo University, Giza 12613, Egypt

4 Laboratory of Laser and New Materials, Department of Physics, Faculty of Science, Cairo University, Giza 12613, Egypt

compounds and is highly dependent on the size and type of the water (Mohammad 2023). Dyes are organic pollutants used in the food and textile industries that negatively affect the aquatic ecosystem, human health, and the environment (Joy Sankar Roy and Messaddeq 2023). With an annual output of 700,000 tons, more than 10,000 types of commercial textile dyes are liberated into watercourses without suitable treatment (Alterkaoui et al. 2022) (Aazam Jafarinejad and Salavati-Niasari 2023). Many traditional physical techniques have been used in the treatment of water contamination such as adsorption, ultrafiltration, photodegradation, and advanced oxidation processes (AOPs) (Shabna SSJD 2023). Currently, photocatalysis, membrane-based methods, sonocatalysis, adsorption, and a diversity of other methods have been utilized to eliminate dyes from water (Shaghayegh Naghdi et al. 2023). Newly, the photocatalysis technology has attracted massive attention because of its energy savings from solar energy utilization, ease of use, low levels of toxic byproducts, environmental protection, and remove dyes from water (Zahoor et al. 2022) (Piyawan Nuengmatcha et al. 2023). Heterogeneous photocatalysis is a well-characterized redox procedure that starts with absorption of light via a semiconductor material (Cruz HBO-O et al. 2023). The following steps manifest in the process (Sridhar et al. 2023): (i) adsorption of reactants on the surface of photocatalyst, (ii) absorption of photons with equal or higher than the band gap, (iii) Electrons move from the valence band (VB) to the conduction band (CB), iv) Transfer of photogenerated electrons (e^-) and holes (h^+) towards the surface of the catalyst, v) Redox reactions with adsorbent substrates, and finally vi) adsorption of the outputs. In photocatalysis, parameters such as photocatalyst dose, band gap, surface area, and production of electron–hole pairs influence the photocatalytic efficiency (Munyai NCH-M. 2023). In the near future, the properties of photocatalysts have been extensively investigated in many environmental applications using semiconductor materials as a photocatalyst to generate reactive species such as (⁻OH) to react with a dye molecule under visible light (Sohier et al. 1963). Semiconductor photocatalysis is widely applied to solve a number of environmental issues such as energy shortage and pollution. Semiconductor photocatalyst materials are well reported because of their remarkable catalytic activity, simplicity, ease of synthesis, cost-effectiveness, and environmental friendliness (Guddappa Halligudra et al. 2023). The catalysts like TiO_2, Fe_3O_4, ZnO, Fe_2O_3 and metal chalcogenides such as CdS, WS_2, SnS_2, MoS_2, ZnS have been utilized to solving inorganic and organic effluents in water (Khatun et al. 2023) (Graphene, inorganic nanocomposites 2023). Among these catalysts, CdS has attracted researchers because of its low toxicity (Gizem Basaran Dindas and Yatmaz 2023). **CdS** is one of the significant (II–VI) semiconductors with wide bandgap, excellent luminescence, and photochemical features (Amiezatul Amirulsyafiee and Harunsani 2023). CdS has the capability to decompose toxic organic compositions due to its wide absorption band in the electromagnetic spectra (Recent progress in photoelectrocatalysis of g-C3N4 for water environment remediation. 2023). However, various problems like large band gap, easy agglomeration, and easy recombination of carriers have been demonstrated in the CdS studies (Zhang et al. 2023). To overcome the above issues, studies have examined a large number of modulations to enhance the photocatalytic efficiency of CdS (Ari Sulistyo Rini et al. 2023). Attempts to develop the photocatalytic performance of CdS have involved changing the structure surface of CdS NPs by dominating morphology, metal/non-metal doping into CdS, depositing CdS to graphene layers, sensitizing enrichment, and crystallinity improvement (Nida Qutub et al. 2022). Gadolinium (atomic number 64) is a metal of the lanthanide group during the rare earth constituents (REEs) combination, which clearly appear in trivalent state (Gd^{3+}) (El-Morsy NSA et al. 2023). Gadolinium oxide (Gd_2O_3) is widely used as an n-type photocatalyst for semiconductors and large bandgap around (5.4) eV (Sugyeong Jeon J-WKaW-BK 2021). Gadolinium oxide (Gd_2O_3) has a relatively high thermal stability, good chemical durability, exhibits features, and low phonon energy identical to those of Fe^{3+} and Al^{3+} that are used to the arsenic removal [(Lingamdinne et al. 2021). In addition, Gd_2O_3 exhibits a magnetic property that can be useful for water recovery using an external magnetic field. In particularly, Gd(III) displays seven unpaired electrons and thus a strong magnet (Lingamdinne et al. 2021). The Gd_2O_3 a good candidate in numerous novel applications such as UV detectors, biomedical devices, luminescent, optical coating, magnetic resonance, fluorescence imaging, high-resolution X-ray medical imaging, and electronic visual displays (El-Morsy NSA 2023). Graphene oxide is a promising nanomaterial which has aroused a massive deal of interest among scientists due to its several features and diversity of applications (Ali et al. 2018). It has two-dimensional (2-D) material, in which the carbon atoms are sp^2 hybridized in a hexagonal lattice (Sukumaran et al. 2018). Graphene oxide (GO) is a zero band gap semiconductor (Yi et al. 2019). It is widely used in optoelectronic devices, photodetectors, energy, drug delivery, and environmental cleaning due to edge effects and the quantum confinement (Jiang et al. 2020). Moreover, GO can absorb co-existing traditional pollutants such as heavy metals and organic contaminants in water due to its large surface areas and considerable functional oxygen groups (Cao et al. 2019). The graphene oxide offer certain characteristics such as good conductivity, excellent optical properties, thermal stability, electrical field resistivity, good lubricating properties, and non-toxicity (Rohan Bahadur and Bando 2023). Many researchers have confirmed that graphene-related nanoparticles such as ZnO,

TiO_2, CdS, and SnO_2, exhibit superior photoreduction properties (Zaman et al. 2022). Methylene blue (MB) is the most commonly used dye for wool and silk. May cause eye burns resulting in permanent eye damage in humans and animals. Inhalation may cause transient shortness of breath or difficulty breathing, while oral ingestion can cause a burning sensation that may lead to nausea, vomiting, profuse sweating, confusion, etc. Therefore, the treatment of wastewater containing such dyes is of concern due to their detrimental effects on receiving water bodies (Kyzas and Kostoglou 2014). The dynamic adsorption process depends on the adsorbate–adsorbent interaction, and the suitability of the system state for water pollution control is investigated (Nafees et al. 2023). Mechanism and response rate are two critical factors in evaluating an adsorption process unit. The residence time necessary for the adsorption reaction to complete is governed by the solute uptake rate, which may be calculated via kinetic analysis. Many kinetic models describe the reaction order of adsorption systems. One of these is the reversible and irreversible Langmuir models. Furthermore, adsorption isotherms are significant in identifying the interaction between the adsorbate and the adsorbent as well as the ideal adsorption capacity of the adsorbent. The adsorption kinetics are best understood by analyzing the adsorption kinetics data (Pan et al. 2023). The purpose of this study is to look at the powder composites of pristine CdS, Gd_2O_3, CdS/Gd_2O_3, and CdS/Gd_2O_3@GO utilized to improve photocatalytic activity, stability, and the capacity to remove MB dyes. The structural, morphological, and optical properties of the resulting composites were investigated using various techniques such as XRD, SEM, and UV–Visible spectroscopy. Different elastic properties of the as-prepared composites were examined using various methods such as the modified Scherrer method, the W–H plot, and the H–W approach based on the broadening of the XRD peak.

Experimental Details

Chemicals and Materials

Cadmium chloride ($CdCl_2$. $2H_2O$) 98%, sodium sulfide (Na_2S) 99.5%, and gadolinium oxide (Gd_2O_3) 99.0% were all acquired from LOBA (India). Sigma–Aldrich (USA) provided the graphene oxide (99.5%), ammonium solution (25%), and deionized water (DI).

Synthesis of Powder Compositions

The co-precipitation method was used to prepare CdS. Separately, 250 mmol of ($CdCl_2$. $2H_2O$) and 90 mmol of (Na_2S) were dissolved in 50 mL of deionized water (DI) with magnetic stirring for 1 h. The ($CdCl_2$. $2H_2O$) solution was then dropped wisely into the (Na_2S) container, while the pH value was kept at 10. Gadolinium oxide (Gd_2O_3) was combined with cadmium sulfide (CdS) and mixed in 50 mL of DI water under highly powerful sonication for 30 min. The solution then was left for precipitation and drying. After that, 50 mg of graphene oxide (GO) and gadolinium oxide (Gd_2O_3) was

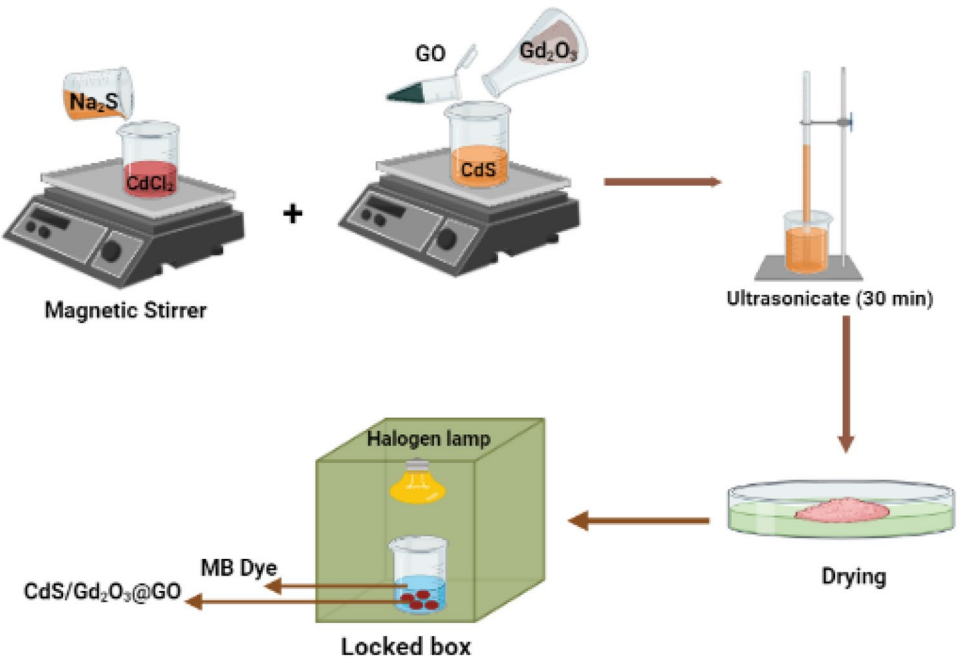

Fig. 1 Preparation of CdS, Gd_2O_3, CdS/Gd_2O_3, and CdS/Gd_2O_3@GO compositions

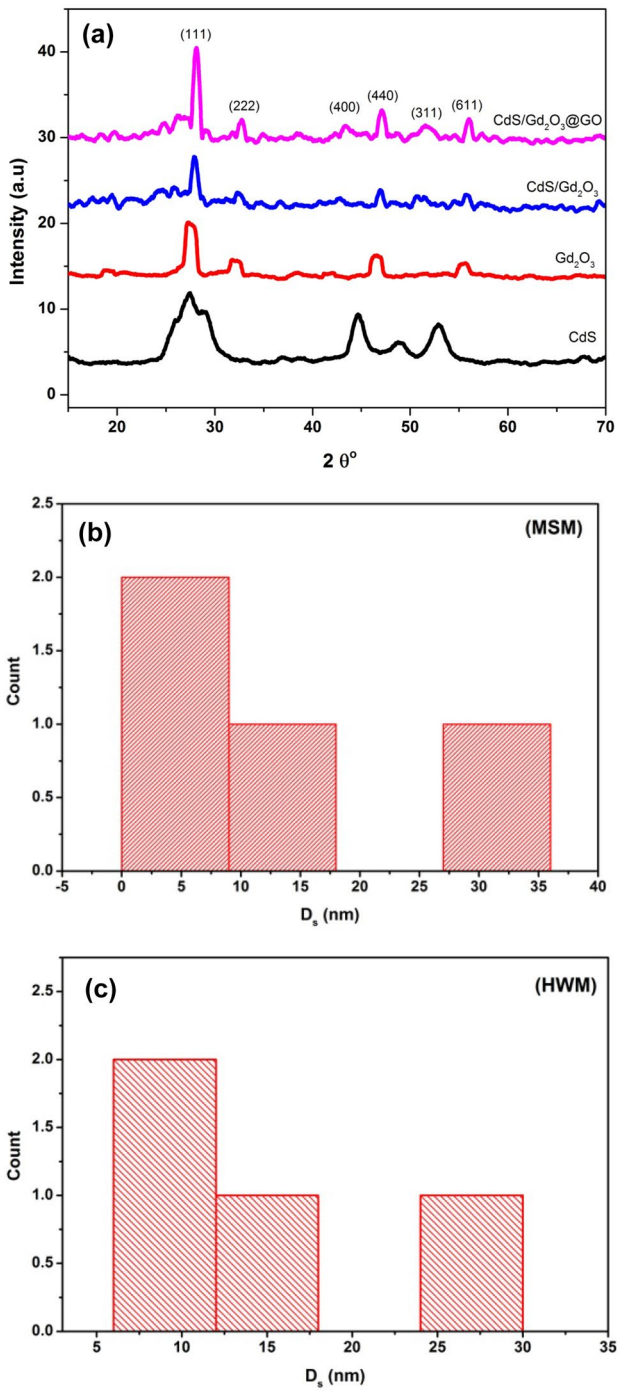

Fig. 2 **a** XRD pattern with different powdered compositions pristine CdS, pure Gd_2O_3, CdS/Gd_2O_3, and CdS/Gd_2O_3@GO and **b**, **c** the crystallite size modified Scherrer model (MSM) and Halder–Wagner method (HWM) and their particle size distribution

added individually to cadmium sulfide (CdS). Finally, the product was dried at 60 °C. Figure 1 depicts the instruments and steps used in sample preparation.

Characterization and Measurements

The crystalline size and the structure were analyzed via the XRD technique (XRD, analytical, Pertpro, Netherlands). The morphology of the composition was examined using Field Emission Scanning Electron Microscope (FE-SEM, QUANTA-FEG250, Netherlands). Furthermore, the particle size distribution was identified by a transmission electron microscope (HRTEM) (JEOL/ JME—2100, Japan). Fourier-transformed infrared (FT-IR) spectra were attained by JASCO-6300 in the range of 4000–400 cm^{-1}, to investigate the functional group of the compound. Thus, UV–Visible Spectroscopy (Bio Aquarius CE 7250, UK) was used to characterize the optical properties of the prepared compositions. Furthermore, XPS has studied the chemical composition of K-ALPHA (Thermo Fisher Scientific, USA).

Dye Degradation Studies

There are several processes for treating solvent extraction, electrolytic reduction, and ion exchange that require the use of more effective remediation technologies such as adsorption, which allows for high pollutant removal percentages. As a photocatalyst, the photocatalytic performance of CdS, Gd_2O_3, CdS/Gd_2O_3, and CdS/Gd_2O_3@GO powdered compositions was calculated. The mixing solution was held in the dark for 60 min prior to lighting to reach adsorption/desorption equilibrium, and the concentration of the solution was measured as the initial concentration (C_o) of the dye solution. The dye degradation experiment was carried out in a closed box at room temperature with a halogen lamp (500W) and a container of 30 mL containing MB (0.5 ppm) and 100 mg of powdered composition. The reaction's progress will be determined by the reactant with a considerably lower concentration. The solution was kept in a dark environment for 60 min, and the halogen lamp was 18 cm away from the compound. A spectrophotometer was used to monitor the 30 mL of MB solution every 10 min.

The degrading activity (%) was estimated using the equation below (Shubha et al. 2023):

$$\eta = \left(\frac{C_o - C}{C_o}\right) x100\%, \quad (1)$$

where $\mathbf{C_0}$ and $\mathbf{C}$ are the first and final concentrations of the dye, respectively.

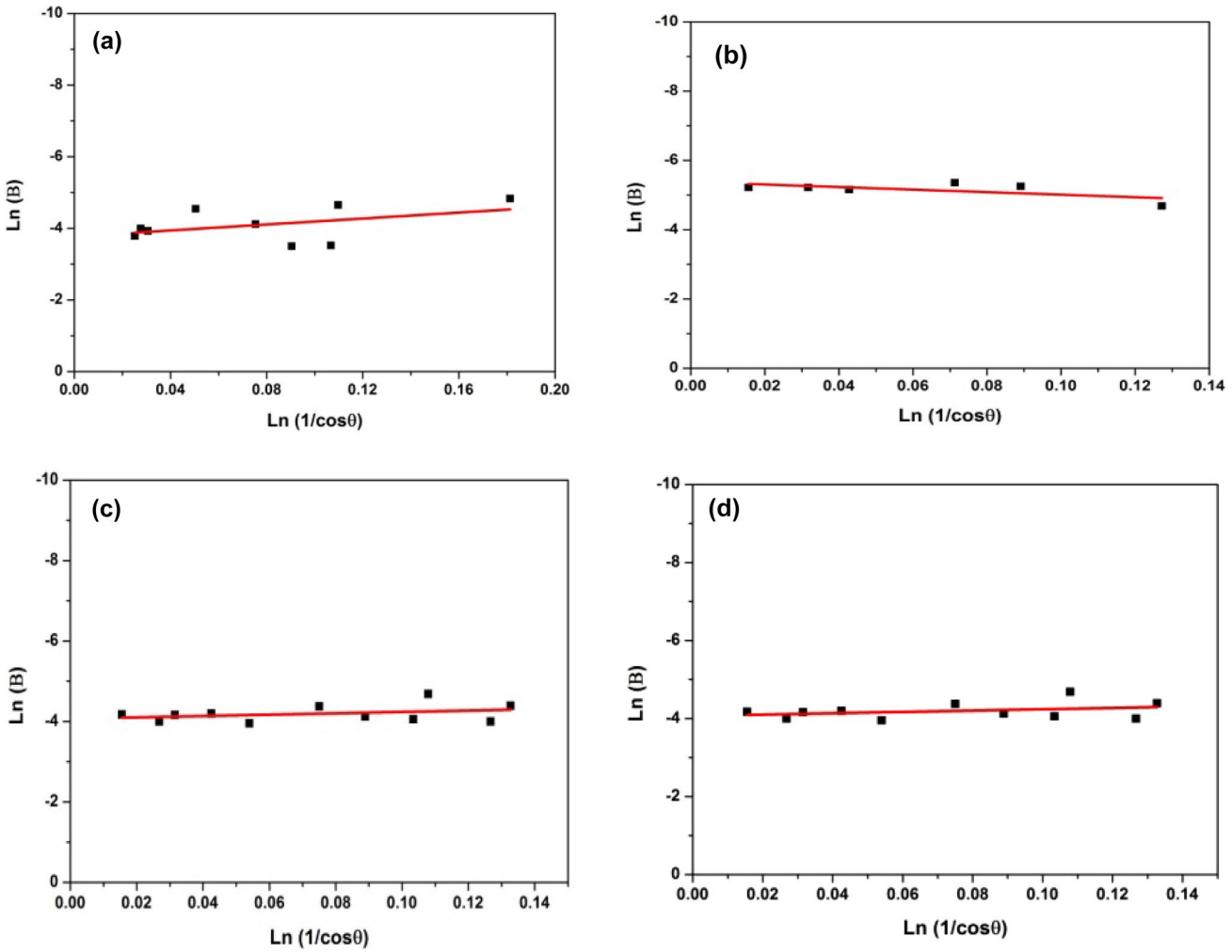

Fig.3 Linear fit plot of modified Scherrer method (MSM) for calculating crystallite size of synthesized (**a**) CdS, (**b**) Gd_2O_3, (**c**) CdS/Gd_2O_3, and (**d**) CdS/Gd_2O_3@GO

Table 1 Results of the modified Scherrer model (MSM) approach for crystallite size, lattice strain, and dislocation density

Composition	D_s (nm)	Micro-strain (ε)	Dislocation density (nm^{-2})×10^{-5}
CdS	6.04	3.88	2.73
Gd_2O_3	30.03	4.63	1.10
CdS/ Gd_2O_3	8.11	4.03	1.52
CdS/ Gd_2O_3@GO	10.46	4.15	9.12

Table 2 Results of the Halder–Wagner for crystallite size, lattice strain, and dislocation density

Composition	D_s (nm)	Micro-strain (ε)×10^{-3}	Dislocation density δ (nm^{-2})×10^{-3}
CdS	7.11	18.3	19.7
Gd_2O_3	29.6	4.3	1.14
CdS/ Gd_2O_3	9.52	11.9	11.00
CdS/ Gd_2O_3@GO	13.21	18.00	5.72

Results and Discussion

X-Ray Powder Diffraction Study

XRD was used to determine the phase structure and crystallite composition of the produced compounds. The XRD patterns of the compositions are depicted in Fig. 2a. Growing grain boundaries may cause grain size to increase when adding CdS to Gd_2O_3 and GO. The presence of CdS deposition causes the size of nanoparticles to increase. The broadening peak of CdS composition denotes that the particles are in small size. The diffraction peaks at 2 Θ^o = 26.5°, 30.7°, 43.9°, and 52.1° indicate that the planes of (111), (200),

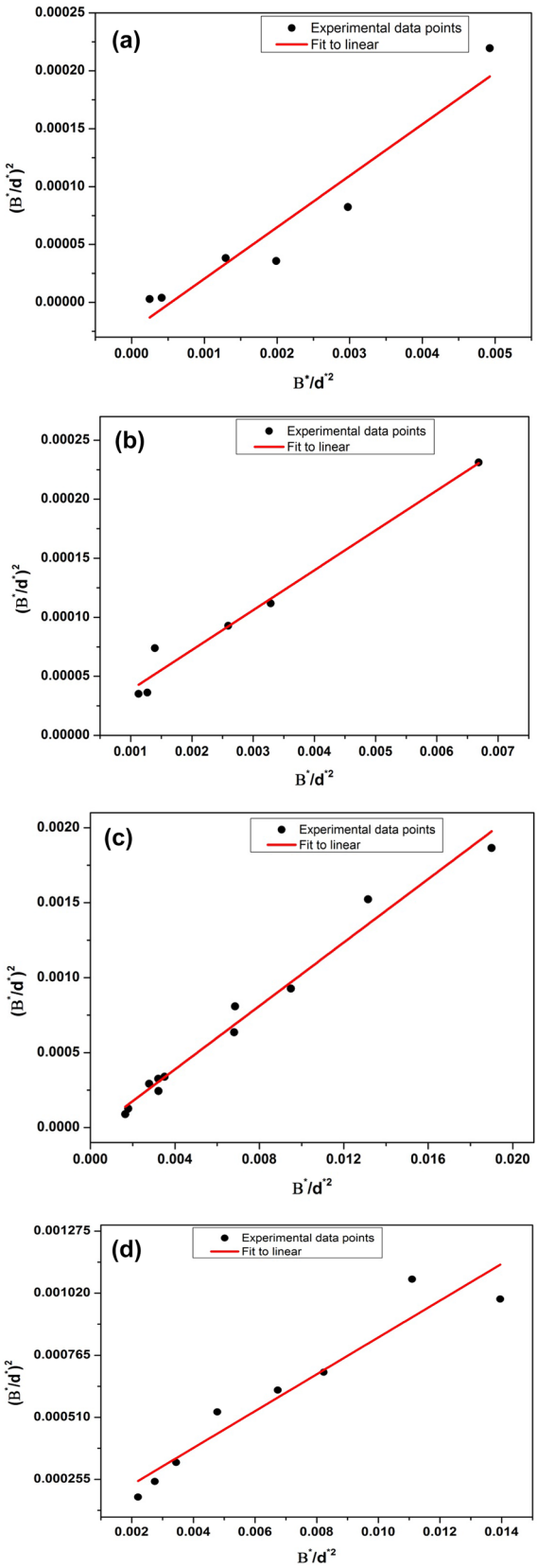

Fig. 4 Linear fit plot of Halder–Wagner method (HWM) for calculating crystallite size of synthesized compositions (**a**) CdS, (**b**) Gd_2O_3, (**c**) CdS/Gd_2O_3, and (**d**) CdS/Gd_2O_3@GO

(220), and (311) are corresponding to cubic symmetry of CdS, according to the ICDD card of (00–042-1411). The diffraction peaks at 2 Θ° = 20.19°, 28.56°, 33.19°, 47.70°, and 52.17°, which correspond to the cubic phase of Gd_2O_3, refer to the planes of (211), (222), (400), (440), and (611), respectively, at reference card (00–043-1014). Furthermore, the peaks estimated at 2Θ = 28.56°, 43.61°, 47.70°, and 52.17° are part of the CdS hexagonal system as (101), (110), (103), and (201) with reference to card (00-006-0314). The weakening and broadening of these diffraction peaks indicated that the CdS/Gd2O3 has a weak crystalline structure, which could reduce the order of structure. Impurities were not observed, indicating that the compounds were synthesized with high crystalline and purity (El-Morsy et al. 2023). Because of the comparatively high crystallinity, the peaks of CdS/Gd_2O_3@GO are sharper than those of CdS. The crystal size, micro-strain, and dislocation density based on the diffraction result were calculated, as detailed in the next section.

The Calculation of Crystallite Size via Various Methods

Modified Scherrer Method (MSM)

Generally, this method was also employed for calculating the crystallite size of compositions. The histogram of particle size distribution is displayed in Fig. 2b. The modified Scherrer equation can be written as follows (Marzieh Rabiei and Monshi 1627):

$$\beta = \frac{K\lambda}{D_s} \times \frac{1}{\cos\theta}, \tag{2}$$

where D_s is the Scherrer's crystallite size (nm), K is the dimensionless shape factor (0.94), λ is the wavelength of X-ray, β is full width at half maximum (FWHM), θ is Bragg's angle, and ε is the micro-strain. Taking logarithm on both sides and the equation becomes:

$$\ln\beta = \ln\frac{K\lambda}{D_s} + \ln\frac{1}{\cos\theta}. \tag{3}$$

Plot of ln β (in y-axis) versus with ln (1/cos θ) (in x-axis) is shown in Fig. 3. The plot's linear fitting can be contrasted with the straight line equation (y = mx + c) used in the following equations. The (Ds) was calculated using Eq. (5). As a result, the crystallite size was calculated to be 30.03 nm (as shown in Table 1).

$$\ln\frac{K\lambda}{D_s} = Interceptor, \frac{K\lambda}{D_s} = e^{(Intercept)}, \tag{4}$$

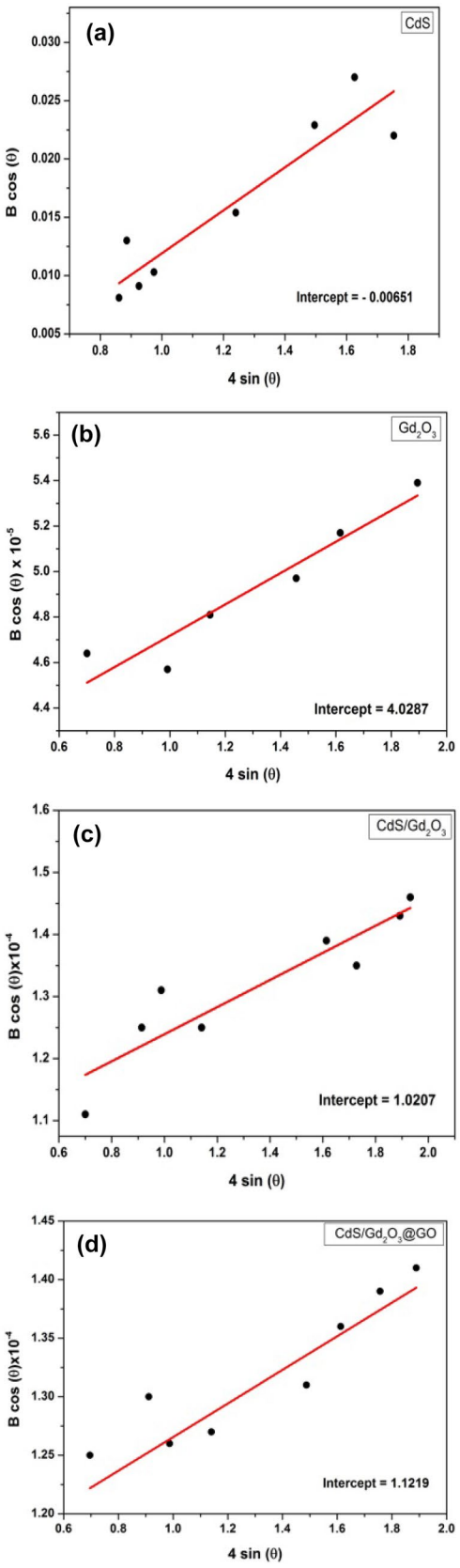

Fig. 5 Linear fit plot of W–H method (WHM) of (**a**) CdS, (**b**) Gd_2O_3, (**c**) CdS/Gd_2O_3, and (**d**) CdS/Gd_2O_3@GO nanocomposite

$$D_s = \frac{K\lambda}{e^{Intercept}}. \tag{5}$$

Table 1 indicates that the average crystallite size according to Modified Scherrer's formula is fluctuated among composites, while the degree of distortion present in the crystalline lattice, micro-strain (ε(values 3.88, 4.63, 4.03, and 4.15 for CdS, Gd_2O_3, CdS/Gd_2O_3, and CdS/Gd_2O_3@GO, respectively, are shown. Dislocation density (δ) is the concentration of dislocation lines per unit area of surface and is proportional to crystal size. Plastic distortion increases the influence of dislocation on material characteristics. The dislocation density was determined using the following formula (Jahil et al. 2022):

$$Dislocationdensity(\delta) = \frac{1}{(D_s)}. \tag{6}$$

The dislocation density is varied from 1.10×10^{-5} to 9.12×10^{-5} for pristine Gd_2O_3 and CdS/ Gd_2O_3@GO.

Halder–Wagner Method (HWM)

Halder–Wagner (HW) investigation is another simplified method for determine the crystallite size (Article Text-2023). The size broadening of the XRD peak profile is neither a Gaussian nor a Lorentzian function (Nath et al. 2020). The results were determined and involved in Table 2, and the particle size distribution histogram is displayed in Fig. 2c. The relationship between the crystallite size and strain according to Halder–Wagner equation (Izumi and Ikeda 2014), is provided by Eq. (7):

$$\left(\frac{\beta^*}{d^*}\right)^2 = \frac{1}{D_s}x\left(\frac{\beta^*}{d^{*2}}\right) + \left(\frac{\varepsilon}{2}\right)^2, \tag{7}$$

$$where, \beta^* = \frac{\beta\cos\theta}{\lambda}, and\ d^* = \frac{2\sin\theta}{\lambda}. \tag{8}$$

Table 2 provides all of the estimated average size values, and the $(\beta^*/d^*)^2$ along the y-axis for each peak of the XRD method is replicated in Fig. 4. The slope of the depicted straight line represents the average size and the intercept represents the compositions' micro-strain. The plot shows that the average particle size for CdS, Gd_2O_3, CdS/Gd_2O_3, and CdS/Gd_2O_3@GO is 7.11, 29.6, 9.52, and 13.21 nm. Whereas the value of micro-strain from Halder–Wagner plot is construct out to be 18.3×10^{-3}, 4.3×10^{-3}, 11.9×10^{-3}, and 18×10^{-3} for CdS, Gd_2O_3, CdS/ Gd_2O_3, and CdS/ Gd_2O_3@GO. The increase in evaluated micro-strain value is actually due to the contribution of mid and low XRD data. Furthermore, the larger strain value obtained in the Halder–Wagner model can be

Table 3 The values of β_{hkl} Cosθ and 4Sinθ via Williamson–Hall method of XRD pattern of CdS

2-θ	*θ*	*β hkl*	*Cos θ*	*β cos θ*	*Sin θ*	*4 sin θ*
26.76	13.38	0.019	0.972	0.019	0.231	0.925
28.18	14.09	0.010	0.969	0.010	0.243	0.974
36.11	18.05	0.016	0.950	0.015	0.309	1.23
43.93	21.96	0.030	0.927	0.027	0.374	1.49
47.99	23.99	0.029	0.913	0.027	0.406	1.62
52.00	26.00	0.009	0.898	0.008	0.438	1.75

attributed to lattice disturbances, which play a significant role in expanding the reflection peaks at low angles (Jahil et al. 2022).

Williamson–Hall Model (WHM)

Williamson–Hall (W–H) method was utilized to determine the crystallite size of the synthesized compounds (Yendrapati et al. 2023). Moreover, W–H model extends a computational path for crystallite size as well as micro-strain (Ahmed et al. 2022). The distortions and imperfections in the crystals of a powdered material cause strain (Lim 2020). In general, the W–H technique expresses the total physical line broadening (FWHM) of an X-ray diffraction peak as a sum of strain and size effects. Clarify the modified W–H plots of the compounds (Manikandan Balakrishnan 2020):

$$\beta_{hkl}\cos\theta = \frac{K\lambda}{D_s} + 4\ \varepsilon\ \sin\theta. \tag{9}$$

Equation 9 is the Williamson–Hall equation for evaluating the lattice strain and crystallite size. In this study, the crystallite size and lattice strain of the composition have been determined using different models such as uniform deformation model (UDM), uniform energy density model (UDEDM), and uniform strain deformation model (USDM). Equation 9 represents the uniform deformation model (UDM), which implicates an isotropic nature of the materials (Pijush et al. 2023). By plotting $\beta_{hkl}\ cos\ \theta$ on the y-axis against $4sin\ \theta$ on the x-axis in presented in Fig. 5. From the slope of the straight line between 4sinθ and $\beta_{hkl}\ cos\theta$, the strain (ε) could be evaluated and the average crystallite size could be evaluated via the intercept of y-axis (Sridhar et al. 2023). The results are listed in Table 3.

$$D_s = \frac{K\lambda}{intercept(y)} \tag{10}$$

Morphology of Powdered Composition

The morphology of CdS/Gd_2O_3 and CdS/Gd_2O_3@GO nanocomposite was exhibited using SEM with different scale bars ranging from 300 to 500 nm, as shown in Fig. 6. The modulation of morphology has a substantial impact on the energy level and electronic structure of CdS/Gd_2O_3@GO, resulting in an increase in photocatalytic activity (Runda Huang and Zhang 2023). As exhibited in Fig. 6a–b, a porous bulk structure and a relatively rough surface with regular spherical particle allocation was identified. In addition, the spherical particles determine the increased roughness and hardness on the bulk surface, which results in a more porous surface area (Farhana Anjum et al. 2023). The grain size as measured from SEM images using Gwyddion software were around 7.4 nm to 85.7 nm. The reduction in particle size is an extra benefit that results in increased surface area (Fatma Mohamed et al. 2023). Figure 6c–d displays that the particles of CdS/Gd_2O_3@GO have shown the irregular shape of particles with the size in the range of 11.1–66.9 nm. SEM analysis shows that particles are in poly-dispersed shape, irregular in form with tendency to form agglomerates and shows the distribution of small and large nanoparticles. The size of these particles is distributed at random on the graphene layer. The particles are particularly agglomerated with few micro-particles (Kannan et al. 2021). The cracks and the surface roughness indicate the porousness of the prepared composites. It indicates the structure of large clusters, low porosity, and disorder distribution.

Table 4 demonstrates the roughness behaviors of the powder compounds, which are exhibited in Fig. 7. Moreover, the peaks could provoke a high trend of cohesion to the ambient surroundings, which encourages the utilization of the compounds for versatile applications (Mamba et al. 2020). Moreover, the parameters R_a, R_t, and R_p are found to follow the change of dislocation density for CdS/Gd_2O_3 and CdS/Gd_2O_3@GO. Whereas R_q, R_v, and R_{tm} are related to micro-strain crystallize size. Generally, the rough surface might develop a photocatalytic activity as compared with the smooth surface which extends fast and effective interaction towards the ambient environment (Zhen Li and Wang

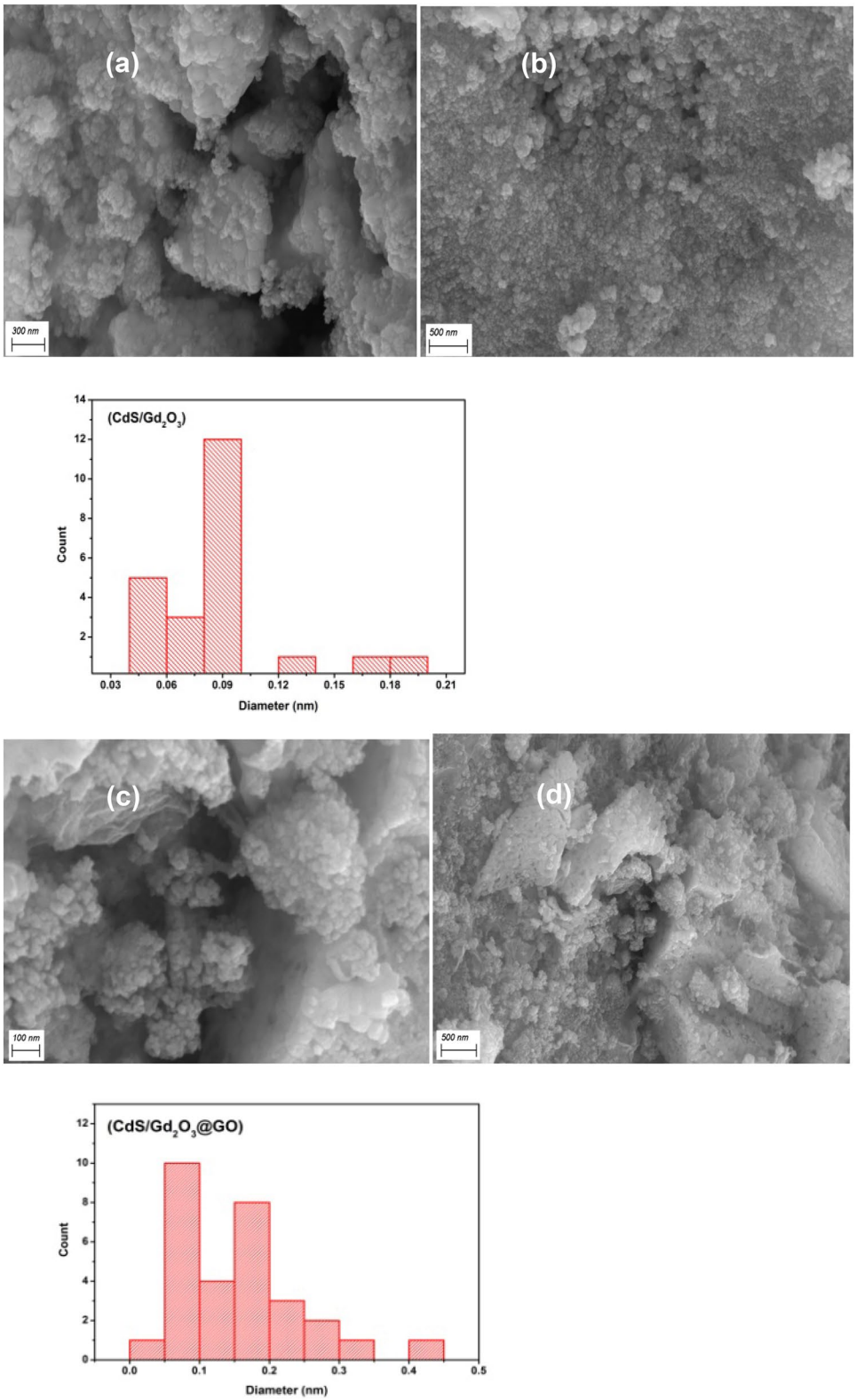

Fig. 6 FE-SEM micrographs of the synthesized composition and the particle distribution: (**a**–**b**) CdS/Gd_2O_3 with varying scale bar started from 300 to 500 nm, (**c**–**d**) CdS/Gd_2O_3@GO with varying scale started from 100 to 500 nm

2023). Furthermore, these nanocomposites can be designed for water purification applications by controlling the morphological features of the surface, which are a function of the structural components (Han et al. 2020).

Table 4 The parameters of surface roughness of the CdS/Gd_2O_3 and CdS/Gd_2O_3@GO, powder compounds

Composition	R_a (nm)	R_q (nm)	R_t (nm)	R_v (nm)	R_p (nm)	R_{tm} (nm)
CdS/Gd_2O_3	4.4	5.6	39.4	16.8	22.6	28.0
CdS/Gd_2O_3@GO	4.24	5.71	38.76	17.46	21.29	33.50

These parameters included Roughness average (R_a), Root mean square roughness (R_q), Maximum height of the roughness (R_t), Maximum roughness valley depth (R_v), Maximum roughness peak height (R_p), and Average maximum height of the roughness (R_{tm})

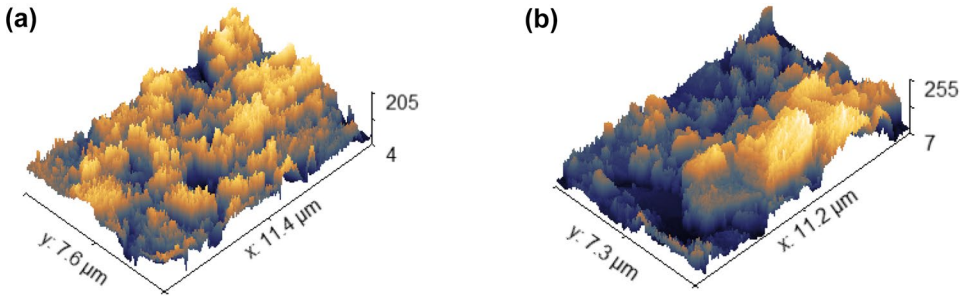

Fig. 7 Surface roughness behaviors: (**a**) CdS/Gd_2O_3, (**b**) CdS/Gd_2O_3 @GO compound

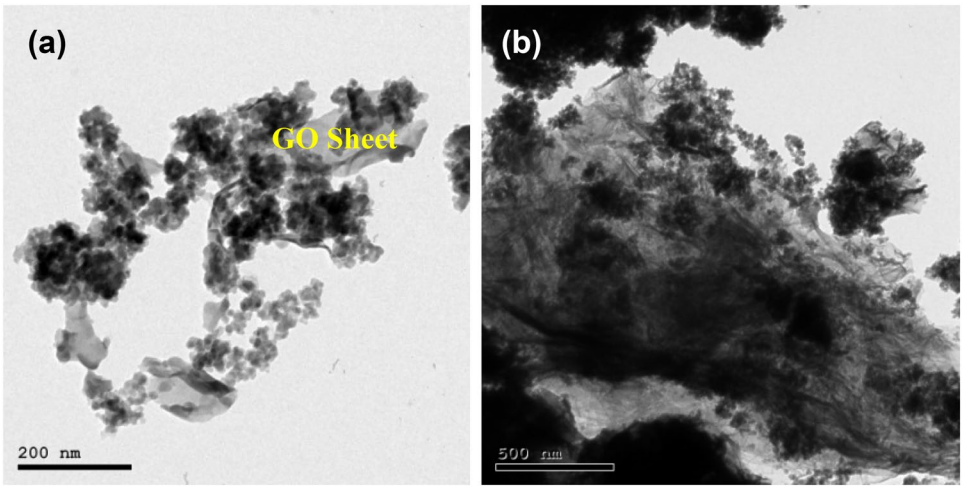

Fig. 8 TEM micrographs of CdS/Gd_2O_3@GO powder composition at several magnifications

Transmission Electron Microscopy

The CdS/Gd_2O_3@GO nanocomposites were also examined via TEM analysis and the results are as shown in Fig. 8a–b at two different magnifications. Highly crystalline CdS/Gd_2O_3@GO nanocomposite of non-uniform geometry with an average particle size of 10 nm in spherical and irregular shaped aggregated nanoparticles are confirmed by TEM images. Moreover, the spherical CdS/Gd_2O_3@GO composition was uniformly supported on the transparent graphene nanosheet, which resemble thin nanosheets and the sheets are partially curved.

FT-IR Analysis

FT-IR analysis was used as a qualitative analysis technique to determine the functional groups present in the synthesized materials (Muraro et al. 2020). Figure 9 shows the FT-IR spectrum ranges between 400 and 4000 cm^{-1} of the synthesized pristine Gd_2O_3, CdS/Gd_2O_3, and CdS/Gd_2O_3@GO. The broadband of 3420 cm^{-1} could be assigned to the stretching vibration mode of O–H. The stretching vibrations of hydroxyl (OH) groups of water adsorbed by the samples were ascribed to the broad peak shown at 3100–3600 cm^{-1}. The band of 1633 cm^{-1} is attributed to H–O–H bending oscillations because the molecules of water are adsorbed on the composite's surface. The exposed band of 1517 cm^{-1} is assigned to the asymmetric vibrational mode belonging to the carboxyl group (C=O). The band 1393 cm^{-1} manifest

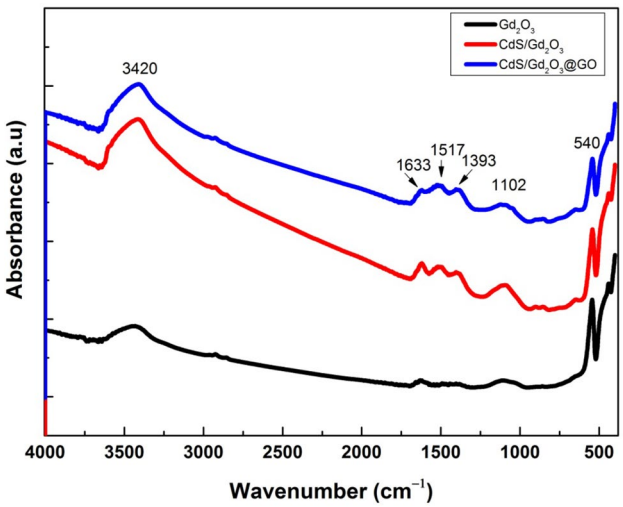

Fig. 9 FT-IR spectra of pristine Gd_2O_3, CdS/Gd_2O_3, and CdS/Gd_2O_3@GO powder compositions

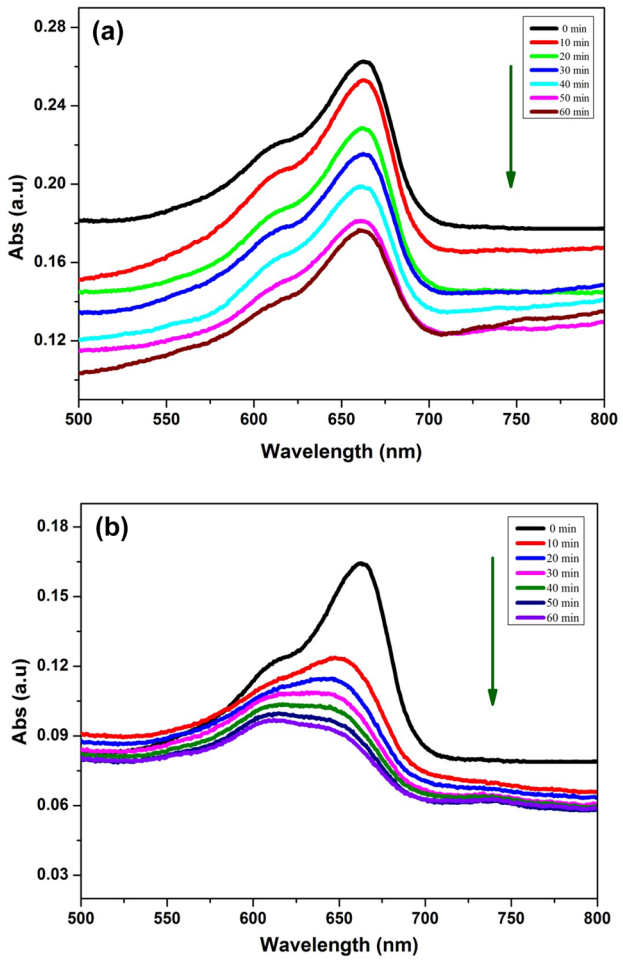

Fig. 10 The absorption spectra of catalyst (**a**) Gd_2O_3 and (**b**) CdS/Gd_2O_3

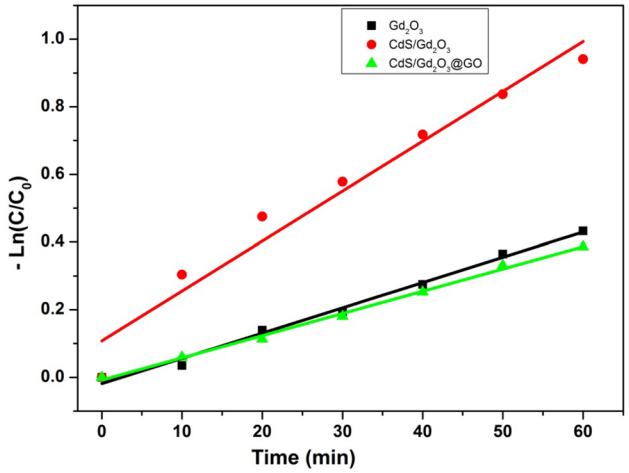

Fig. 11 Kinetics of photocatalytic efficiency of Gd_2O_3, CdS/Gd_2O_3, and CdS/Gd_2O_3@GO

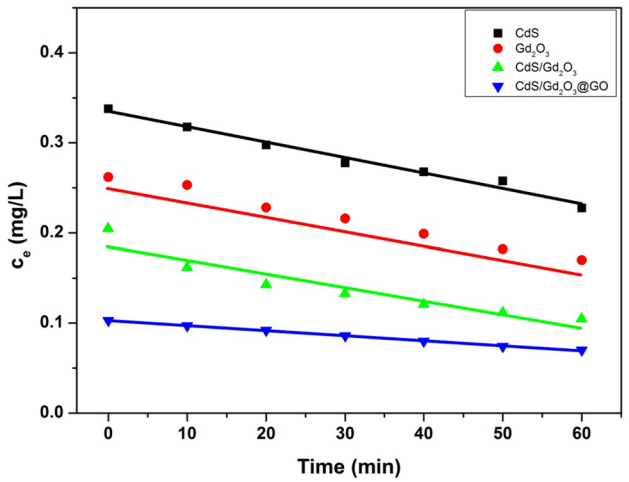

Fig. 12 Concentration versus time plots for the composition

the C–O bending. The band at 540 cm^{-1} is ascribed to Gd–O stretching at Gd_2O_3, respectively.

Photocatalytic Activity Investigation of Methylene Blue (MB) Dye

The decomposition of methylene blue is widely used as an example to describe the effectiveness of photocatalysts in a wastewater treatment process (Barakat et al. 2023). Methylene blue (MB) is often used as a type dye molecule for photocatalytic degradation characterization of semiconductors. The obtained composition was allowed to resolve the photo catalytic performance via the photo degradation process with MB dye under visible light. Figure 10a, b explicates

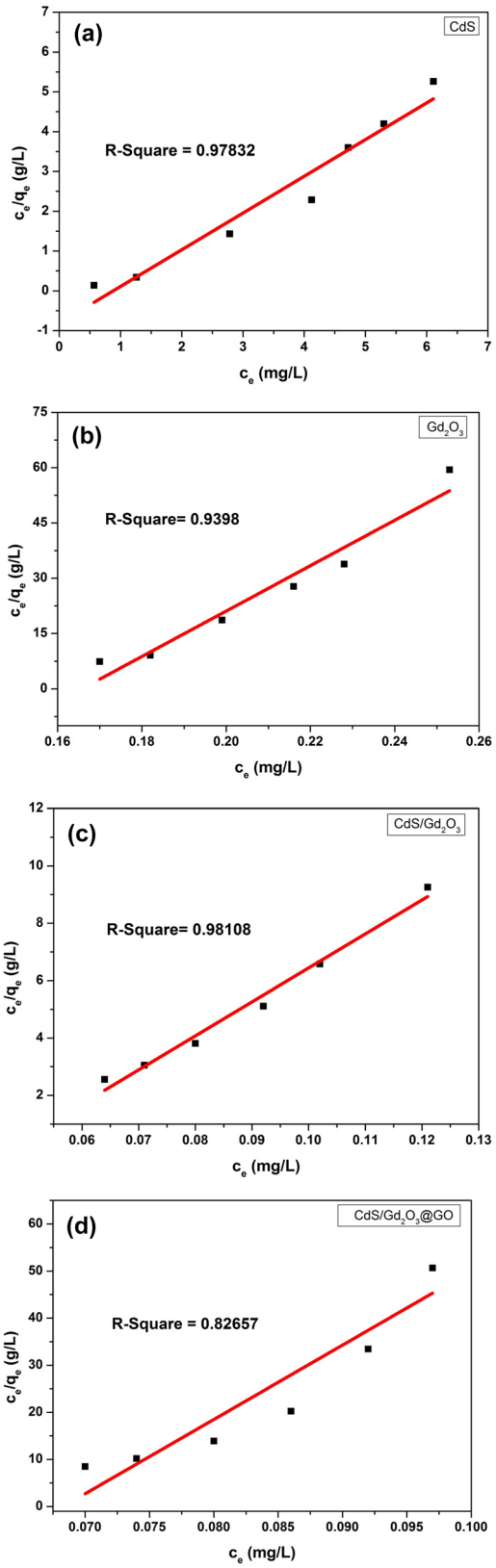

Fig. 13 (**a**–**d**) Plot between c_e/q_e on y-axis and c_e on x-axis

the absorption spectra of the MB solutions with catalysts Gd_2O_3 and CdS/Gd_2O_3 to visible light illumination. A sharp decrease in the absorbance was observed in the presence of catalysts due to photo degradation of the dye. With increasing irradiation time, the absorbance steadily decreases in the presence of catalysts (Shakeel Khan et al. 2023). To analyze the photo catalytic properties of the synthesized catalysts and the reaction kinetics of compositions the Langmuir–Hinshelwood model for pseudo-first-order reaction (Yao et al. 2021) is used. Photo catalytic degradation kinetics can be quantified by the following equation (Keke et al. 2023) (Fig. 11):

$$\ln\left(\frac{C}{C_o}\right) = -K_{app}t, \tag{11}$$

$$LnC = LnC_o - K_{app}t, \tag{11-a}$$

where C_o is the initial concentration of the MB at $t=0$, C is the dye's concentration at different interval times, and K_{app} is the reaction rate constant (Liao et al. 2022). To analyze such kinetic, the quantity -Ln (C/C_0) was plotted as a function of the irradiation time for different composites, Fig. 11. In this way, the pseudo-first-order degradation kinetics was observed for all applied catalysts. The reaction rate (degradation rate) is accelerated to clean MB contaminated water under visible light irradiation (Saravanan and Mika 2023). Figure 12 depicts the effect of dye concentration on the degradation of MB dye over time. The fit plots revealed are all straight lines, indicating that the photo catalytic degradation is strong.

The quantity q_t of the adsorbed die was calculated using equation:

$$q_t = \frac{(C_i - C_e)V}{M}, \tag{12}$$

where q_t is the amount of adsorbed die molecules (mg/g) at time t, C_e is the concentration (mg/L) at time t, C_o is the initial concentration (mg/L), V is the volume of working solution, and M is the mass of catalyst.

The maximum adsorption value (q_{max}) was calculated to determine the conversion capacity using the following equation (Abbas and Trari 2020):

$$q_{tmax} = \frac{(C_i - C_e)V}{M}, \tag{13}$$

where q_{max} acts to the optimal adsorbed quantity of MB.

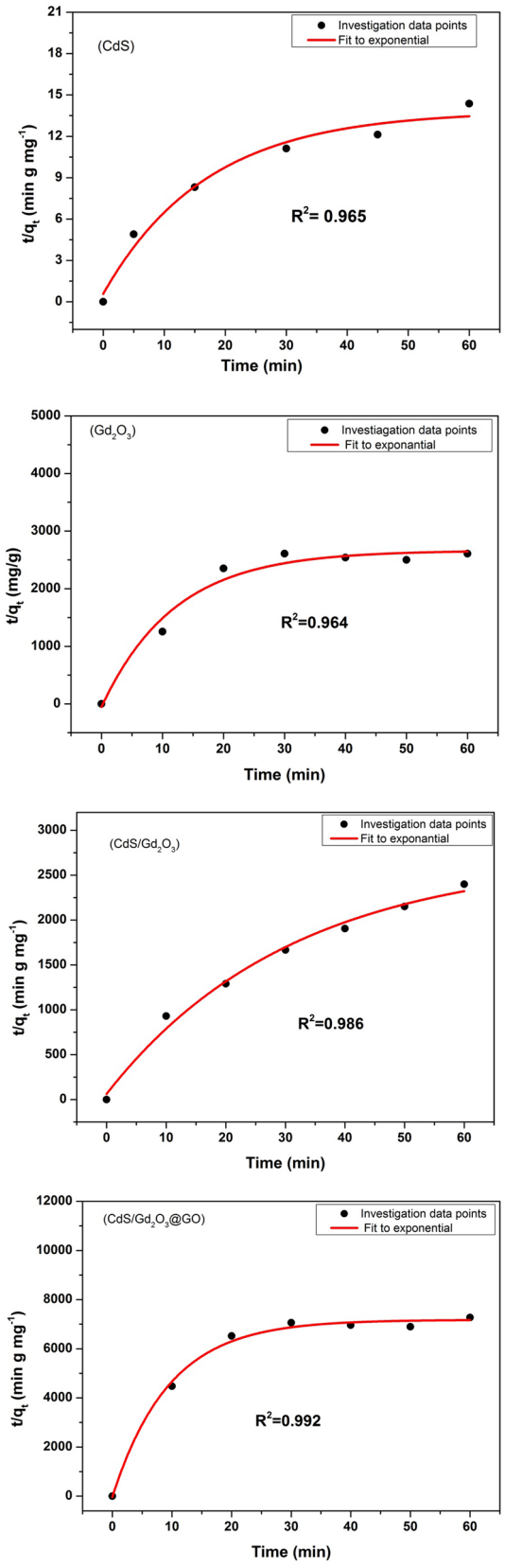

Fig. 14 The exponential fitting forms of pseudo-second-order model (type 1)

Adsorption Isotherms

Adsorption isotherms are quite helpful in understanding the adsorption process. The Langmuir isotherm estimates the maximal adsorption capacity assuming that the adsorbent's surface is encompassed by a monolayer of adsorbent molecules (Ho 2006). The adsorption isotherm reflects qualitative information about the nature of the adsorbent surface contact, as well as the particular relationship between adsorbate concentration and the degree of accumulation on the adsorbent surface at constant temperature (Mina Ghorbani et al. 2023). Adsorption isotherms are crucial in maximizing adsorbent utilization; thus, examining isothermal data using various isothermal models is a critical step in determining the optimal model that may be used for design goals. (EnyewAmareZerefa SMJa. 2023). Although many factors influence adsorption capacity, such as initial adsorbate concentration, reaction temperature, solution pH value, adsorbent particle size and dose, and solute nature, a kinetic model is only concerned with the effect of observable parameters on the overall rate (Enhancing the TiO2-Ag 2023). Adsorption of metal ions, dyes, oils, and organic compounds from aqueous solutions has been successfully accomplished using the pseudo-second-order expression (Gama et al. 2006).

Pseudo-First-Order (PFO) Model PFO describes the adsorption of solutes on adsorbents by a first-order mechanism. The Langmuir isotherm model is based on the assumption of a monolayer and uniform absorbed energy. The Langmuir constant (K_L) and maximum adsorption capacity (q_{max}) are determined from the intercept and slope of the linear Langmuir Eq. 14. R^2 is close to 1, which is a strong correlation coefficient. The intercept and slope of the C_e/q_e versus C_e plot can be used to calculate q_m and K_L values is indicated in Fig. 13. The expression for the nonlinear form of the Langmuir isotherm is shown in the following equation (Williams and EKF 2023):

$$\frac{c_e}{q_e} = \frac{1}{q_m K_L} + \frac{c_e}{q_m}, \tag{14}$$

where K_L denotes the Langmuir adsorption constant and q_m is the maximum adsorption capacity.

Adsorption Kinetic Analysis

Adsorption kinetics provides valuable information about possible: Adsorption mechanisms and their potentially rate-limiting steps in the adsorption process. It is also an important step to select the best conditions for optimizing parameters and large-scale removal process, in aqueous media (Abbas and Trari 2020).

Table 5 Parameters of pseudo-second-order model

Pseudo second order					Pseudo second order			
Type 1					Type 2			
Composition	q_e (mg/g)	k_2	R^2	h	q_e (mg/g)	k_2	R^2	h
CdS	5	0.012	0.965	0.324	6.448	0.005	0.904	0.228
Gd_2O_3	0.067	0.108	0.964	0.0005	− 0.024	0.380	0.928	0.0002
CdS/Gd_2O_3	0.027	3.541	0.986	0.0026	0.047	0.558	0.825	0.0012
CdS/Gd_2O_3@GO	0.012	1.678	0.992	0.0002	0.114	0.011	0.977	0.0002

Pseudo-Second-Order (PSO) Model The PSO model assumes that the rate of solute adsorption is proportional to the available sites on the adsorbent. The reaction rate depends on the amount of solute on the surface of the adsorbent. In the form of the PSO Eq. 15, the driving force (q_m–q_t) is proportional to the number of active sites available on the sorbent.

$$\frac{dq_t}{d_t} = k_2(q_m - q_t)^2, \tag{15}$$

where q_t is adsorbate adsorbed onto adsorbent at time t (mg/g), q_m is equilibrium adsorption capacity (mg/g), and k_2 is PSO rate constant. Equation (15) has been treated and rearranged into the forms of Eqs. (15-a) & (15-b). Furthermore, adsorption kinetics influences the rate of solute adsorption, which in turn governs the desorption reaction's survival time (EnyewAmareZerefa SMJa. 2023). To resolve the kinetics survey of MB, the pseudo-second-order model was used (Niazi et al. 2022). Second-order models are used to fit the photo catalytic oxidation of various dyes (En Shi et al. 2023). We utilized the following two kinetic models to investigate the dye adsorption techniques, Eqs. (15-a)&(15-b) (Alexander Agafonov et al. 2023):

$\frac{t}{q_t} = \frac{1}{k_2 q_e^2} + \frac{t}{q_e}$, (Type 1, plotting t/q_t against t) (15-a),

$\frac{1}{q_t} = \left(\frac{1}{k_2 q_e^2}\right)\frac{1}{t} + \frac{1}{q_e}$, (Type 2, plotting $1/q_t$ against 1/t) (15-b).

Equations (15-a and 15-b) show the pseudo-second-order kinetic model, where k_2 is pseudo-second-order rate constant. The slope 1/qt and intercept $1/k_2q^2e$ in t versus t/q^2_e plot was used to determine the values of the parameters of the pseudo-second-order kinetic model. However, Eq. (15-a) was found to provide better fitting results in curvilinear function compared to other forms. This behavior is compatible with the adsorption isotherms model's type-I behavior. It shows a monolayer formation tendency, achieving saturation of the adsorption surface. The adsorption mechanism was determined to be chemisorption, which involves electron transfer between the adsorbate and adsorbent (Md. Kamrul Hossain MMHaSA. 2023).

The initial sorption rate was calculated using second-order rate constants (h) (Niazi and Tanvir Shahzad. 2022) and is given by the following equation:

$$h = k_2 q_e^2. \tag{16}$$

While the pseudo-second-order model fitted to the highest R^2 value as shown in Figs. 14 & 15. The results of pseudo-second-order kinetic models are summarized in Table 5.

The pseudo-second-order model plot is illustrated in Figs. 14 and 15. The determine parameters are displayed in Table 5. The maximum adsorption capacity (q_e) determined for CdS, Gd_2O_3, CdS/ Gd_2O_3, and CdS/ Gd_2O_3@GO adsorption for type 1 were 5, 0.067, 0.027, and 0.012 mg/g. The R^2 values originated from the pseudo-second-order (type 2) plots for CdS, Gd_2O_3, CdS/ Gd_2O_3, and CdS/ Gd_2O_3@GO were 0.904, 0,928, 0.825, and 0.977, respectively. The initial sorption rate (h) is varied values from type 1 and type 2. Thus, the pseudo-second-order rate constant (k_2) is ranged from 0.005 for CdS to 0.011 for CdS/ Gd_2O_3@GO in type 2 (Table 5), fitting the experimental data to pseudo-second-order kinetics yielded type 2 better correlation coefficients (R^2) than fitting the experimental data to pseudo-second-order kinetics type 1 for all the systems survived.

Adsorption Thermodynamic Study

The MB dye adsorption process was assessed to determine the thermodynamic feasibility of the thermal effects of adsorption; the standard Gibbs free energy change (G°) was

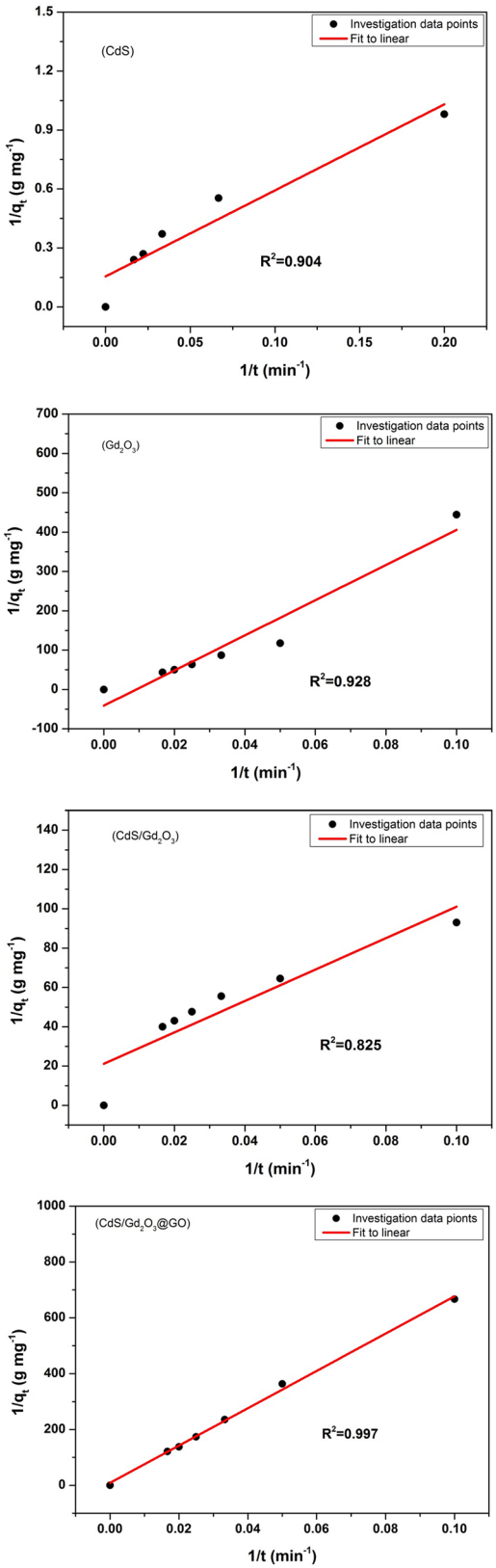

Fig. 15 The linear forms of pseudo-second-order model (type 2)

Table 6 The values of Gibbs functions (ΔG°) for adsorption of MB dye on the different catalysts

Catalyst	K_d	Ln K_d	ΔG (KJ.mol^{-1})
CdS	1.982	0.684	− 1706.69
Gd_2O_3	0.0605	− 2.804	6995.07
CdS/Gd_2O_3	0.202	− 1.59734	3984.07
CdS/Gd_2O_3@GO	0.054	− 2.90699	7250.61

calculated using the Van't Hoff (EnyewAmareZerefa SMJa. 2023) Eq. (17):

$$\Delta G = RTLnK_d, \tag{17}$$

where K_d is the distribution coefficient of adsorption and equal to the ratio between adsorption capacity (q_e) to the equilibrium concentration (C_e); T is the solution's temperature (27 + 273) in Kelvin (°K) and R is the gas constant (8.314 J/mol K).

To assess the spontaneity and feasibility of adsorption processes, the Gibbs free energy of change is utilized. A negative ΔG^0 value confirms a spontaneous process, whereas a positive ΔG^0 value confirms a non-spontaneous process (Table 6). This study showed that the magnitudes of the Gibbs free energy were nearly constant during the adsorption process. The result for the current study indicates a negative value of ΔG^0 in the case of CdS—1706 kJ mol^{-1}. In other circumstances, the values range between 3984.07 and 7250 kJ mol^{-1}.

Photo Catalytic Degradation Mechanism

The mechanism of photo catalytic MB degradation of the composition is presented in Fig. 16. During visible light irradiation, absorb light with energy equal to or greater than its band gap energy and electrons (e^-) are excited from valence band (VB) to conduction band (CB) and a pair (e^- & h^+) is formed. Resultantly, the electrons in CB react with O_2 to generate superoxide radicals, whereas holes in the VB react with the molecules of water absorbed on catalyst surface to create hydroxyl radicals ($^{\bullet}OH^{\cdot}$), and the hydroxyl radicals are strong oxidizing species, which through oxidative mechanism converts the dye molecule into low molecular weight intermediates The generated hydroxyl and superoxide radicals react with MB to degrade it into CO_2 and H_2O and hence the MB contaminated water becomes clean (Effect of dopant on ferroelectric 2023).

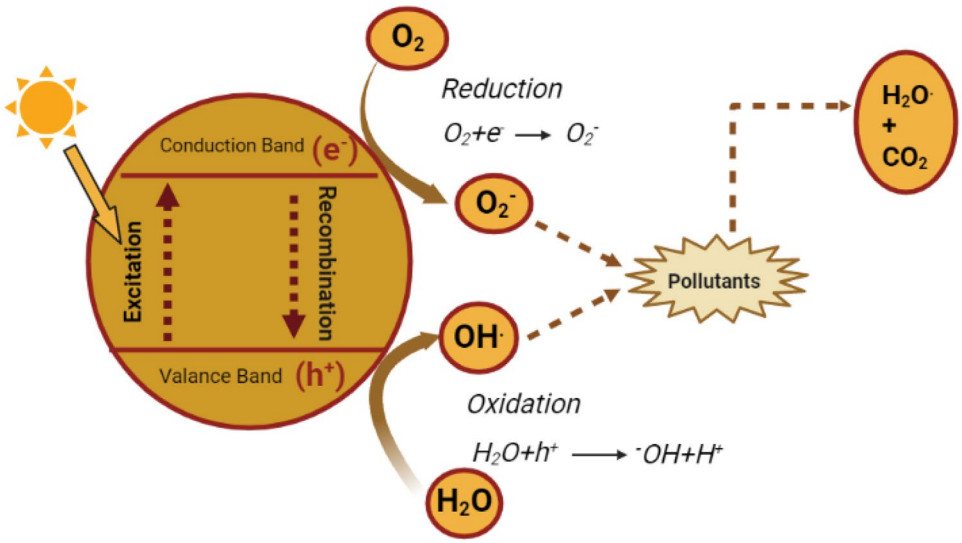

Fig. 16 Schematic mechanism of photocatalytic degradation of MB

Conclusion

The compositions were synthesized successfully via the co-precipitation method. Different techniques were used to calculate the average crystallite size using XRD spectra. Using the Scherrer plot, Williamson–Hall plot, and Halder–Wagner method, XRD peak broadening analysis has been carried out to explore the various elastic properties of the compositions, including intrinsic strain and dislocation density. According to the Halder–Wagner plot, the average particle size for CdS, Gd_2O_3, CdS/ Gd_2O_3, and CdS/ Gd_2O_3@GO is 7.11, 29.6, 9.52, and 13.21 nm. Because the equations for the Halder–Wagner approach are derived from the straight line fitting in the diagram, the results are highly accurate. There is a convergence between the outcomes of the Halder–Wagner method and the outcomes of the other methods, namely the Williamson–Hall method and the Modified Scherrer equation, which rely on the graph to predict the crystal size and micro-strain. The findings also show that the adsorption mechanisms exhibit pseudo-second-order dynamics. Pseudo-second-order kinetic models were used to fit and interpret kinetic data. The benefit of utilizing this model is that the equilibrium capacity can be derived from the model as well as the initial adsorption rate, eliminating the need to know it from the tests. The Gibbs free energy change (ΔG^o) is varied between —1706 and 7250 kJ mol^{-1}.

Funding Open access funding provided by The Science, Technology & Innovation Funding Authority (STDF) in cooperation with The Egyptian Knowledge Bank (EKB).

Data availability Data will be made available on request.

Open Access This article is licensed under a Creative Commons Attribution 4.0 International License, which permits use, sharing, adaptation, distribution and reproduction in any medium or format, as long as you give appropriate credit to the original author(s) and the source, provide a link to the Creative Commons licence, and indicate if changes were made. The images or other third party material in this article are included in the article's Creative Commons licence, unless indicated otherwise in a credit line to the material. If material is not included in the article's Creative Commons licence and your intended use is not permitted by statutory regulation or exceeds the permitted use, you will need to obtain permission directly from the copyright holder. To view a copy of this licence, visit http://creativecommons.org/licenses/by/4.0/.

References

Aazam Jafarinejad HB, Salavati-Niasari M (2022) Sonochemical synthesis and characterization of CuInS2 nanostructures using new sulfur precursor and their application as photocatalyst for degradation of organic pollutants under simulated sunlight. Arab J Chem 15:104007.

Abbas M, Trari M (2020) Contribution of adsorption and photo catalysis for the elimination of Black Eriochrome (NET) in an aqueous medium-optimization of the parameters and kinetics modeling. Scientific African 8:e00387

Ahmed MT, Islam S, Ahmed F, Nayak M (2022) Comparative study on the crystallite size and bandgap of perovskite by diverse methods. Adv Condensed Matter Phys 2022:1–7

Alexander Agafonov AE, Larionov A, Sirotkin N, Titov V, Khlyustova aA (2022) Sorption and photocatalytic characteristics of composites based on Cu–Fe oxides. Physchem 2:305–20

Ali AA, Nazeer AA, Madkour M, Bumajdad A, Al SF (2018) Novel supercapacitor electrodes based semiconductor nanoheterostructure of CdS/rGO/CeO 2 as efficient candidates. Arab J Chem 11:692–699

Alterkaoui A, Eskikaya O, Gün M, Yabalak E, Arslan H, Dizge N (2022) Production of waste tomato stem hydrochar (TS-HC) in subcritical water medium and application in real textile wastewater using photocatalytic treatment system. Int J Environ Res 16:110

Amiezatul Amirulsyafiee MMK, Mohammad Hilni Harunsani (2022) Ag3PO4 and Ag3PO4–based visible light active photocatalysts: recent progress, synthesis, and photocatalytic applications. Catalysis Commun 172:106556

Ari Sulistyo Rini APD, Dewi R, Jasril YR (2023) Biosynthesis of nanoflower Ag-doped ZnO and its application as photocatalyst for Methylene blue degradation. Materials Today
<576-Article Text-985–1–10–20210402.pdf>.
Bin Fang ZX, Sun D, Li Z, Zhou W (2022) Hollow semiconductor photocatalysts for solar energy conversion. Adv Powder Mater 1:100021
Cao X, Ma C, Zhao J, Musante C, White JC, Wang Z et al (2019) Interaction of graphene oxide with co-existing arsenite and arsenate: adsorption, transformation and combined toxicity. Environ Int 131:104992
Catalina Nutescu Duduman CGdC, Gabriela Antoaneta Apostolescu, Gabriela Ciobanu DL, Favier L, Harja M (2022) Enhancing the TiO2-Ag Photocatalytic Efficiency by Acetone in the Dye Removal fromWastewater. Water 14:2711
Cruz HBO-O D, Flores-Espinosa RM, Ávila Pérez P, Ruiz-López II, Quiroz-Estrada KF (2022) Synthesis of Ag/TiO2 composites by combustion modified and subsequent use in the photocatalytic degradation of dyes. J King Saud Univ—Sci 34:101966.
El-Morsy NSA MA, Ibrahium HA, Alharbi W, Alshahrani MY, Menazea AA (2022) Optimizing the mechanical and surface topography of hydroxyapatite/Gd2O3/graphene oxide nanocomposites for medical applications. J Saudi Chem Soc 26:101463
En Shi XW, Zhang M, Wang X, Gao J, Zheng Y, Zhu X (2022) Synthesis and enhanced visible-light photocatalytic activity of anatase TiO2/sludge-derived activated carbon composite for degradation of methylene blue. Int J Electrochem Sci 17.
EnyewAmareZerefa SMJa. Preparation and photocatalysis of ZnO/bentonite based on adsorption and photocatalytic activity. Mater Res Express 2023;10:035502.
Farhana Anjum AMA, Ali Khan M, Khan MI, Sher Bahadar Khan KA, Bakhsh EM, Alamry KASYA (2021) Sudip Chakraborty. Photo-degradation, thermodynamic and kinetic study of carcinogenic dyes via zinc oxide/graphene oxide nanocomposites. J Mater Res Technol 15:3171e91
Fatma Mohamed MS, Aljohani G, Ahmed AM (2021) Synthesis of novel eco-friendly CaO/C photocatalyst from coffee and eggshell wastes for dye degradation. J Mater Res Technol 14:3140e9.
Fenfen Liang HW, Yub R, Liu C, Wang Y, Bai L, Hao C, Hao G (2022) Recent progress in photoelectrocatalysis of g-C3N4 for water environment remediation. Progress Nat Sci 32:538–53
Gama EM, da Silva LA, Lemos VA (2006) Preconcentration system for cadmium and lead determination in environmental samples using polyurethane foam/Me-BTANC. J Hazard Mater 136:757–762
Gizem Basaran Dindas DYK-I, Huseyin Cengiz Yatmaz (2022) A novel Fe/HNT visible light-driven heterogeneous photocatalyst: Development as a semiconductor and photocatalytic application. Progress Nat Sci 32:273–81.
Gopalan Saianand A-IG, Wang L, Venkatramanand K, Roy VAL, Sonar P, Lee D-E, Naidu R (2022) Conducting polymer based visible light photocatalytic composites for pollutant removal: Progress and prospects. Environ Technol Innovation 28:102698
Guddappa Halligudra CCP, Gururaj R, Giridasappa A, Sabbanahalli C, Ananda Kumar Channapillekoppalu Siddegowda AKMR, Dinesh Rangappa PDS (2022) Magnetic Fe3O4 supported MoS2 nanoflowers as catalyst for the reduction of p-nitrophenol and organic dyes and as an electrochemical sensor for the detection of pharmaceutical samples. Ceramics Int 48:35698–707
Hajra Ahsan MHS, Hussain S, Shahid M, Shahbaz M, Ali HM, Imran M, Ayyub M, Mahmood F, Niazi MBK, Shahzad T (2022) Photocatalysis and adsorption kinetics of azo dyes by nanoparticles of nickel oxide and copper oxide and their nanocomposite in an aqueous medium. PeerJ
Han YW, Qu M, Zhong S, Han M, Yang L, Liu H, Su Y, Lei B (2020) Ziqiang. Ag@AgCl quantum dots embedded on Sn3O4 nanosheets towards synergistic 3D flower-like heterostructured microspheres for efficient visible-light photocatalysis. Ceramics Int 46:24060–70
Ho YS (2006) Review of second-order models for adsorption systems. J Hazard Mater 136:681–689
Ismat Bibi MQ, Ata S, Majid F, Kamald S, Alwadai N, Sultan MFR, Iqbal S, Iqbal M (2021) Effect of dopant on ferroelectric, dielectric and photocatalytic properties of chromium-doped cobalt perovskite prepared via micro-emulsion route. Results Phys 20 103726
Irié Bi Irié Williams EKF, Pomi Bi Boussou Narcisse, Aka Alla Martin, Koffi Koffi Kra Sylvestre, Trokourey Albert and Zhen Gu (2022) Study of Photocatalytic Activity of a Nanostructured Composite of ZnS and Carbon Dots. Advances in Nanoparticles 11:111–28
Izumi F, Ikeda T (2014) Implementation of the Williamson-Hall and Halder-Wagner Methods into RIETAN-FP. 3:33–38
Jahil SS, Mohammed IA, Khazaal AR, Jasim KA, Harbbi KH (2022) Application the halder—wagner to calculation crystal size and micro strain by x-ray diffraction peaks analysis. NeuroQuantology 20:199–204
Jiang Z, Lei Y, Zhang Z, Hu J, Lin Y, Ouyang Z (2020) Nitrogen-doped graphene quantum dots decorated ZnxCd1-xS semiconductor with tunable photoelectric properties. J Alloy Compd 812:152096
Joy Sankar Roy SM, Messaddeq Y (2021) Ultrafast cleaning of methylene blue contaminated water accelarating photocatalytic reaction rate of the BiVO 4 nanoflakes under highly intense sunlight irradiation. J Photochem Photobiol 7:100037.
Kannan K, Radhika D, Gnanasangeetha D, Krishna LS, Gurushankar K (2021) Y3+ and Sm3+ co-doped mixed metal oxide nanocomposite: Structural, electrochemical, photocatalytic, and antibacterial properties. Appl Surface Sci Adv 4:100085
Keke Guan JLa, Lei W, Wang H, Tong Z, Jia Q, Zhang HSZ (2021) Synthesis of sulfur doped g-C3N4 with enhanced photocatalytic activity in molten salt. Journal of Materiomics 7: 1131e42
Khatun A, Suhag MH, Tateishi I, Furukawa M, Katsumata H, Kaneco S (2023) Facile synthesis of ZnO/g-C3N4 with enhanced photocatalytic performance for the reduction of Cr(VI) in presence of EDTA under visible light irradiation. Int J Environ Res 17:32
Kyzas GZ, Kostoglou M (2014) Green adsorbents for wastewaters: a critical review. Materials 7:333–364
Liao X, Li TT, Ren HT, Zhang X, Shen B, Lin JH et al (2022) Construction of BiOI/TiO2 flexible and hierarchical S-scheme heterojunction nanofibers membranes for visible-light-driven photocatalytic pollutants degradation. Sci Total Environ 806:150698
Lim NAMaMRR DJ Universal scherrer equation for graphene fragments. 2020
Lingamdinne LP, Lee S, Choi J-S, Lebaka VR, Durbaka VRP, Koduru JR (2021) Potential of the magnetic hollow sphere nanocomposite (graphene oxide-gadolinium oxide) for arsenic removal from real field water and antimicrobial applications. J Hazard Mater 402:123882
Liyun Yana JT, Qiao Q-a, Wang Y, Cai H, Jin J, Gaob H, Xu Y (2023) Synthesize, construction and enhanced performance of Bi2WO6/ZnS heterojunction under visible light: experimental and DFT study. Arab J Chem 16:104760
Mamba G, Gangashe G, Moss L, Hariganesh S, Thakur S, Vadivel S et al (2020) State of the art on the photocatalytic applications of graphene based nanostructures: from elimination of hazardous

pollutants to disinfection and fuel generation. J Environ Chem Eng 8:103505
Manikandan Balakrishnan RJ (2020) Properties of sol-gel synthesized multiphase TiO2 (AB)-ZnO (ZW) semiconductor nanostructure: an effective catalyst for methylene blue dye degradation. Iran J Catalysis 10(1):1–16
Marzieh Rabiei AP, Monshi A, Nasiri S, Janusas AVaG (2020) Comparing methods for calculating nano crystal size of natural hydroxyapatite using x-ray diffractio. Nanomaterials 10:1627
Md. Kamrul Hossain MMHaSA (2023) Studies on synthesis, characterization, and photocatalytic activity of TiO2 and Cr-doped TiO2 for the degradation of p-chlorophenol. ACS omega 8:1979−88.
Mina Ghorbani SS, Abdizadeh H, Reza Golobostanfard M (2023) Modified BiFeO3/rGO nanocomposite by controlled synthesis to enhance adsorption and visible-light photocatalytic activity. J Mater Res Technol 22:1250e67
Mohammad T, ALSamman JSn (2021) Recent advances on hydrogels based on chitosan and alginate for the adsorption of dyes and metal ions from water. Arab J Chem 14:103455
Mujeeb Khana MEA, Tahir MN, Khan M, Ashraf MRH M, Khan M, Varala R, Nujud Mohammed Badawi SFA (2022) Graphene/inorganic nanocomposites: Evolving photocatalysts for solar energy conversion for environmental remediation. J Saudi Chem Soc 26:101544
Munyai NCH-M S (2021) Green derived metal sulphides as photocatalysts for waste water treatment. A review. Curr Res Green Sustain Chem 4:100163
Muraro PCL, Mortari SR, Vizzotto BS, Chuy G, Dos Santos C, Brum LFW et al (2020) Iron oxide nanocatalyst with titanium and silver nanoparticles: synthesis, characterization and photocatalytic activity on the degradation of Rhodamine B dye. Sci Rep 10:3055
Nafees Ahmad DB, Jabeen S, Ahmad N, Iqbal A, Waris Abdul Hakeem Anwer CJ (2023) Insight into the adsorption thermodynamics, kinetics, and photocatalytic studies of polyaniline/SnS 2 nanocomposite for dye removal. J Hazardous Mater Adv 10:100321.
Nasser AM, Barakat GMKT, Khalil KA (2022) Methylene blue dye as photosensitizer for scavenger-less water photo splitting: new insight in green hydrogen technology. Polymers 14:523
Nath D, Singh F, Das R (2020) X-ray diffraction analysis by Williamson-Hall, Halder-Wagner and size-strain plot methods of CdSe nanoparticles- a comparative study. Mater Chem Phys 239:122021
Nida Qutub PS, Sabir S, Sagadevan S, Oh W-C (2022) Enhanced photocatalytic degradation of Acid Blue dye using CdS/TiO2 nanocomposite. Sci Rep 12:5759
Pan M, Zhang M, Zou X, Zhao X, Deng T, Chen T, et al. (2019) The investigation into the adsorption removal of ammonium by natural and modified zeolites: kinetics, isotherms, and thermodynamics. Water SA 45
Pijush CH, Dey SS, Das R (2020) X-ray diffraction study of the elastic properties of jagged spherical CdS nanocrystals. Mater Sci-Poland 2:271–8
Piyawan Nuengmatcha AK, Porrawatkul P, Pimsen R, Chanthai S, Nuengmatcha P (2023) Efficient degradation of dye pollutants in wastewater via photocatalysis using a magnetic zinc oxide/graphene/iron oxide-based catalyst, Water Sci Eng 1.
Rohan Bahadur GS, Bando Y, Vinu A (2022) Advanced porous borocarbonitride nanoarchitectonics: Their structural designs and applications. Carbon 190:142–69.
Runda Huang JW, Menglong Zhang, Baiquan Liu, Zhaoqiang Zheng, Dongxiang Luo. Strategies to enhance photocatalytic activity of graphite carbon nitride-based photocatalysts. Materials & Design 2021;210:110040.
Saravanan Gengan HCAM, Sillanp¨a M, Nhat T (2022) Carbon dots and their application as photocatalyst in dye degradation studies- Mini review. Results Chem 4: 100674
Shabna S SSJD, Biju CS (2023) Potential progress in SnO2 nanostructures for enhancing photocatalytic degradation of organic pollutants. Catalysis Commun 177: 106642.
Shaghayegh Naghdi MMS, Zendehbad M, Djahaniani H HK, Eder D (2023) Recent advances in application of metal-organic frameworks (MOFs) as adsorbent and catalyst in removal of persistent organic pollutants (POPs). J Hazardous Mater 442:130127
Shakeel Khan AN, Khan I, Muhammad M, Sadiq M, Muhammad aN (2023) Photocatalytic degradation of organic dyes contaminated aqueous solution using binary CdTiO2 and ternary NiCdTiO2 nanocomposites. Catalysts 13: 44
Shubha JPBR, Patil RC, Khan M, Shaik MR, Alaqarbeh M, Alwarthan A, Abdulnasser Mahmoud Karami SFA (2023) Facile synthesis of ZnO/CuO/Eu heterostructure photocatalyst for the degradation of industrial efflue. Arab J Chem 16:104547
Sohier A, El-Hakam FTA, Salama RS, Gamal S, Abo El-Yazeed WS, Ibrahim AA, Ahmed AI (2022) Application of nanostructured mesoporous silica/bismuth vanadate composite catalysts for the degradation of methylene blue and brilliant green. J Mater Res Technol18:1963–76
Sridhar APS, Saravanakumar K, Sankaranarayanan RK (2023) Dual doping effect of Ag+ & Al3+ on the structural, optical, photocatalytic properties of ZnO nanoparticles. Appl Surface Sci Adv 13:100382.
Sugyeong Jeon J-WKaW-BK (2021) Synthesis of Gd2O3 nanoparticles and their photocatalytic activity for degradation of Azo dyes. Catalysts 11:742
Sukumaran SS, Rekha CR, Resmi AN, Jinesh KB, Gopchandran KG (2018) Raman and scanning tunneling spectroscopic investigations on graphene-silver nanocomposites. J Sci 3:353–358
Yao C, Chen W, Li L, Jiang K, Hu Z, Lin J et al (2021) ZnO: Au nanocomposites with high photocatalytic activity prepared by liquid-phase pulsed laser ablation. Opt Laser Technol 133:106533
Yendrapati Taraka Prabhu KVR, Sai Kumar VS, Siva Kumari B (2014) X-ray analysis by williamson-hall and size-strain plot methods of ZnO nanoparticles with fuel variation. World J Nano Sci Eng 4:21–8
Yi Z, Liu L, Wang L, Cen C, Chen X, Zhou Z et al (2019) Tunable dual-band perfect absorber consisting of periodic cross-cross monolayer graphene arrays. Results Phys 13:102217
Zahoor U, Rameel MI, Javed AH, Khan MA, Al-Humaidi JY, Iqbal S et al (2022) Yttrium doped bismuth vanadate titania heterojunction for efficient photoreduction of Cr from wastewater under visible light. Int J Environ Res 16:88
Zaman N, Iqbal N, Noor T (2022) Advances and challenges of MOF derived carbon-based electrocatalysts and photocatalyst for water splitting: a review. Arab J Chem 15:103906
Zhang S, Cai M, Wu J, Wang Z, Lu X, Li K et al (2023) photocatalytic degradation of TiO2 via incorporating Ti3C2 MXene for methylene blue removal from water. Catal Commun 174:106594
Zhen Li DJ, Wang Z (2020) ZnO/CdSe-diethylenetriamine nanocomposite as a step-scheme photocatalyst for photocatalytic hydrogen evolution. Appl Surface Sci 529